CHEMISTRY OF MATERIALS
Cite This: Chem. Mater. 2019, 31, 4769−4778
Article
pubs.acs.org/cm

$KBaTeBiO_6$: A Lead-Free, Inorganic Double-Perovskite Semiconductor for Photovoltaic Applications

Arashdeep Singh Thind,[†] Shalinee Kavadiya,[‡] Mojgan Kouhnavard,[‡] Robin Wheelus,[†] Sung Beom Cho,[§,¶] Liang-Yi Lin,[‡] Clayton Kacica,[‡] Hemant Kumar Mulmudi,[∥] Kinga A. Unocic,[⊥] Albina Y. Borisevich,[⊥] Ghanshyam Pilania,[#] Pratim Biswas,[‡] and Rohan Mishra*[,§,†]

[†]Institute of Materials Science & Engineering, [‡]Department of Energy, Environmental and Chemical Engineering, and [§]Department of Mechanical Engineering & Materials Science, Washington University in St. Louis, One Brookings Drive, St. Louis 63130, Missouri, United States

[∥]Research School of Electrical, Energy and Materials Engineering, College of Engineering and Computer Science, Australian National University, Canberra 2601, Australia

[⊥]Center for Nanophase Materials Sciences, Oak Ridge National Laboratory, Oak Ridge 37831, Tennessee, United States

[#]Materials Science and Technology Division, Los Alamos National Laboratory, Los Alamos 87545, New Mexico, United States

Supporting Information

ABSTRACT: Solar cells made up of lead-halide perovskites have shown a remarkable increase in power conversion efficiency; however, they are plagued with instability issues that, combined with the toxicity of lead, have led to a search for new semiconductors made up of heavy and nontoxic metals such as bismuth. Here, we report on a new, inorganic, double perovskite oxide semiconductor: $KBaTeBiO_6$, which has an experimental indirect band gap of 1.88 eV and shows excellent stability. We combined data analytics and high throughput density functional theory calculations to search through thousands of hypothetical inorganic double perovskite oxides containing bismuth and predict $KBaTeBiO_6$ as a potential photovoltaic material, which was subsequently synthesized using a wet-chemistry route. The calculated effective mass of the charge carriers for $KBaTeBiO_6$ is comparable to the best performing Bi-halide double perovskites. Our work demonstrates the untapped potential of inorganic Bi-based double perovskite oxides—that offer the ability to change both the cation combination and their stoichiometry to achieve desired electronic properties—as exciting, benign, and stable alternatives to lead-halide perovskites for various semiconducting applications.

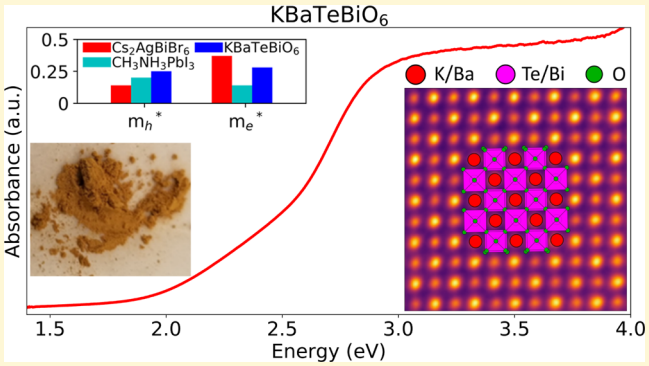

INTRODUCTION

Lead-halide perovskites have been an area of extensive research since the observation of the photovoltaic effect in $CH_3NH_3PbI_3$ and $CH_3NH_3PbBr_3$ in 2009.[1] The power conversion efficiency of these perovskites has now reached 22.7%;[2] however, they show poor stability and degraded performance on exposure to sunlight and moisture.[3−5] While effective encapsulation methods and processing routes, such as electrospray deposition have demonstrated enhanced stability, change to a more stable composition is still desirable.[6] Additionally, the use of lead, a toxic element, raises questions of potential toxicity.[7] Therefore, there is an ongoing search to find stable and environmentally benign alternatives to lead-halide perovskites. The substitution of lead with lighter group IV cations, such as Sn and Ge, has yielded limited success because of the instability of the +2 oxidation state in these cations.[8,9] The heavy Pb^{2+} cation with its occupied $6s^2$ lone-pair electrons is pivotal to attain an electronic structure that facilitates efficient charge collection and makes them optimal for solar cell applications.[10] The delocalized nature of the Pb 6p states leads to a highly dispersed conduction band with a low effective mass of the electrons. The valence band edge is formed of antibonding states of Pb $6s^2$ hybridized with the p-states of the halide anions, which reduce the effective mass of the holes. Moreover, the presence of antibonding states at the valence band edge results in defect levels that are either shallow or lie within the bands.[11] The Pb $6s^2$ lone-pair electrons also result in a large dielectric constant that improves carrier lifetimes by effectively screening charged defects and by reducing the exciton binding energies.[12] Overall, the combination of a large dielectric constant and the presence of antibonding states at the valence band edge have been

Received: March 13, 2019
Revised: June 11, 2019
Published: June 11, 2019

Downloaded via AJOU UNIV on February 3, 2026 at 03:24:55 (UTC).
See https://pubs.acs.org/sharingguidelines for options on how to legitimately share published articles.

© 2019 American Chemical Society

DOI: 10.1021/acs.chemmater.9b01025
Chem. Mater. 2019, 31, 4769−4778

attributed to the remarkable defect tolerance that these lead-halide perovskites exhibit.[11−15]

It is attractive to replace Pb^{2+} with an isoelectronic and nontoxic cation such as Bi^{3+}. Many of the bismuth-halide semiconductors proposed recently for photovoltaic applications have a layered structure with broken BiX_6 octahedral connectivity along one or more crystallographic directions, which result in flat electronic bands.[16−18] To improve the dispersion of the bands, a three-dimensional (3D) connectivity of the BiX_6 octahedra,[19] as observed in the perovskite structure, is required; however because of charge neutrality reasons, it is not possible to obtain defect-free halide perovskites with a Bi^{3+} cation. Recently, double perovskite halides with a stoichiometry of A_2BBiX_6, where A is a larger monovalent cation, B is a smaller monovalent cation that alternatively occupies the octahedral site with Bi, and X is a halide ion have been proposed as potential alternatives.[20−24] Examples include $Cs_2AgBiBr_6$,[21,22] $Cs_2AgBiCl_6$,[22] and $(CH_3NH_3)_2AgBiBr_6$.[24] These double perovskite halides have highly dispersed valence and conduction bands[22] and show large carrier lifetimes comparable to lead-halide perovskites.[21] However, all the reported $ABBiX_6$ double perovskites have an indirect band gap that in most cases is within 2−3 eV, which restricts efficient utilization of the solar spectrum. Of the reported compounds, $Cs_2AgBiBr_6$ is most promising having an indirect band gap of 1.95 eV.[21,22] Furthermore, these compounds are observed to degrade over a period of few weeks on exposure to ambient air and light with the degradation being more severe for $Cs_2AgBiBr_6$.[22] Finally, the use of monovalent halides restricts the composition space for combining different A and B cations to achieve the desired properties.[20]

To overcome the abovementioned challenges and achieve stable compounds containing Bi^{3+} cations within a 3D-octahedral framework having a low band gap suitable for photovoltaic applications, we have explored the family of double perovskite oxides with a general stoichiometry of $A'A''B'BiO_6$. Based on charge neutrality conditions, one can obtain a vast composition space of 29,515 unique $A'A''B'BiO_6$ double perovskites. Previously, cation substitution has been demonstrated to vary the band gap in oxide perovskites from 1.1 to 3.8 eV,[25,26] which indicates the possibility to obtain low-band gap $A'A''B'BiO_6$ double perovskites. However, a search of the inorganic crystal structure database (ICSD)[27] for $A'A''B'BiO_6$ leads to only 28 unique compounds, with a nearly equal stoichiometry of all the four cations. To rapidly discover stable promising compounds from the vast composition space, we have used a combination of high-throughput density functional theory (DFT) calculations and data analytics. We have used a linear regression model based on the octahedral (o) and tolerance factors (t) of the experimentally observed $A'A''B'BiO_6$ compounds to screen hypothetical compounds that are expected to be stable. Subsequently, we have used DFT calculations to identify thermodynamically stable $A'A''B'BiO_6$ compounds and their electronic structures. Of the several new $A'A''B'BiO_6$ compounds that we find to be theoretically stable, we predict $KBaTeBiO_6$ to have an indirect theoretical band gap of 1.94 eV with highly dispersed conduction and valence bands. The predicted band gap and effective masses of the charge carriers in $KBaTeBiO_6$ are comparable to $Cs_2AgBiBr_6$. Finally, we have synthesized $KBaTeBiO_6$ nanoparticles using a wet-chemistry approach, which shows excellent stability for over a year under ambient conditions (no glove box). We confirm the formation of a perovskite phase for $KBaTeBiO_6$ using X-ray powder diffraction (XRD) and aberration-corrected scanning transmission electron microscopy (STEM). We obtain an experimental indirect band gap of 1.88 eV, in good agreement with the theoretical predictions. Finally, we have fabricated photoelectrochemical (PEC) solar cell devices using $KBaTeBiO_6$ nanoparticles. These first-generation solar cells, that have not been optimized, show an average efficiency of 0.04%. Overall, our work opens a vast new composition space of environmentally benign bismuth-oxide perovskites that offer large tunability of their optoelectronic properties to obtain high-performance semiconductors for various applications.

METHODS

Computational Details. DFT calculations were performed using the Vienna Ab initio Simulation Package (VASP)[28] using the projector-augmented-wave method.[29] We employed generalized gradient approximation (GGA) as implemented in the Perdew−Burke−Ernzerhof (PBE) functional[30] for crystal and electronic structure optimization. The enforcement of layered and rock-salt ordering at the A and B sites, respectively, lead to a 20-atom supercell having two formula units (f.u.) of the double perovskite. This supercell is a $\sqrt{2} \times \sqrt{2} \times 2$ transformation of a typical 5-atom ABX_3 perovskite primitive unit cell. The initial lattice parameters for geometric optimization (a, b, and c) were approximated from the Slater's atomic radii such that $a = b = 2\sqrt{2}(r\mathrm{B} + r\mathrm{X})$ and $c = 4(r\mathrm{B} + r\mathrm{X})$. We used a plane-wave basis set with a cutoff energy of 400 eV for the coarse and fine relaxation steps, and 520 eV for the final static total energy calculation step. The Brillouin zone was sampled using a Gamma-centered Monkhorst−Pack[31] k-points mesh while keeping the k-points per reciprocal atom at ∼8000 for the fine relaxation and the single-step static calculation. The fine relaxation and the static calculation were carried out in accordance with pseudopotentials and other DFT settings employed by Open Quantum Materials Database (OQMD).[32] For the hybrid Heyd-Scuseria-Ernzerhof (HSE06) functional calculations, the fraction of Hartree−Fock exchange (α) was fixed at 0.25, and an inverse screening length of 0.207 $Å^{-1}$ was used.

Synthesis and Characterization. $KBaTeBiO_6$ was synthesized using a simple wet-chemistry route. KNO_3 (Fisher Scientific, USA), $Ba(NO_3)_2$ (Sigma-Aldrich, USA), $Te(OH)_6$ (Sigma-Aldrich, USA), and $Bi(NO_3)_3{\cdot}5H_2O$ (Alfa Aesar, USA) were used as the precursors for each element. A solution of each precursor was prepared separately in deionized water, except for $Bi(NO_3)_3{\cdot}5H_2O$, which was prepared in HNO_3 and water mixture (1:3 ratio of HNO_3/H_2O). An equimolar mixture solution with 0.1 M concentration of these precursors was then prepared in nitric acid. The precursor mixture was dried overnight (12 h) in a muffle furnace at 100 °C. After complete drying, the dried precursor powder (∼0.31 g in one batch) was annealed at 650 °C for 6 h (time after reaching the desired temperature). Thermogravimetric and differential thermal analyses (TA Instruments, New Castle, DE) were performed to choose a proper temperature for annealing based on the decomposition profile of the precursors. The annealed powders were characterized to investigate crystal structure, optical properties (band gap), and elemental composition. Crystal structure information was obtained using an X-ray diffractometer (XRD, Bruker D8 ADVANCE, Bruker, USA) in Bragg−Brentano geometry, configured with a 1.5418 Å Cu X-ray under an operating condition of 40 kV. Analysis of the XRD pattern and peak search was performed using the DIFFRACTION.-SUITE Eva software. The absorption and reflection spectra of the double perovskite (thin film on a glass slide) were measured using a UV−vis spectrophotometer (UV-2600, Shimadzu, USA) with an integrating sphere (ISR-2600 Plus, Shimadzu, USA) over 300−900 nm with a step size of 0.5 nm. Elemental composition was determined using scanning transmission electron microscope (STEM; JEOL 2200FS) field-emission STEM/TEM instrument equipped with a

DOI: 10.1021/acs.chemmater.9b01025
Chem. Mater. 2019, 31, 4769−4778

CEOS GmbH (Heidelberg, Ger) corrector operated at an acceleration voltage of 200 kV. The microscope is equipped with a Bruker-AXS silicon-drift detector system (SDD) to utilize energy-dispersive X-ray spectroscopy (EDS) methods such as elemental mapping. The elemental X-ray hypermaps were acquired with a nominal beam current of 200 pA to optimize the count rate for acquisition. The sample was prepared using $KBaTeBiO_6$ in hexane solution on lacey carbon films on copper TEM grids.

The atomic resolution STEM imaging was carried out at Oak Ridge National Laboratory using the aberration-corrected Nion UltraSTEM 200 microscope operated at 200 kV, which is equipped with a fifth-order aberration corrector and a cold field-emission electron gun. $KBaTeBiO_6$ powder was dispersed on a lacey carbon TEM grid using dip-casting. The TEM grids were heated to 160 °C in vacuum to remove excess solvent and contamination. To accurately determine the atomic positions of atomic columns in high-angle annular dark-field (HAADF) images, Gaussian blurring was used to smooth out the HAADF images.

Fabrication of PEC Solar Cells. $KBaTeBiO_6$ powder was used to prepare $KBaTeBiO_6$ solution by two methods. In the first method, $KBaTeBiO_6$ powder was mixed with ethanol and water in a ratio of 2:1 followed by a few minutes of sonication and stirring. In the second method, $KBaTeBiO_6$ solution was prepared following a previously reported method,[33,34] where acetic acid, water, and ethanol were added dropwise to the obtained powder and were ground well with mortar and pestle for approximately 30 min. Then, terpineol and ethyl cellulose solution in ethanol (5%) were added as binders. The mixture was again ground well and transferred to a vial with excess ethanol for a few minutes of stirring and sonication.

For the device fabrication, the $KBaTeBiO_6$ solution was drop-casted on a TiO_2 opaque electrode (Solaronix, Australia), which consists of TiO_2 nanoparticles (15−20 nm and >100 nm), which consist of a screen-printed active transparent layer of Ti-nanoxide covered by a reflective layer of Ti-nanoxide resulting in an overall TiO_2 layer thickness between 12 and 16 μm. The TiO_2 film was then annealed at 450 °C for 30 min before coating the $KBaTeBiO_6$ layer. The $KBaTeBiO_6$ solution was drop-casted on the TiO_2 electrode followed by annealing at 100 °C for 15 min for the first solution and 400 °C for 30 min for the second $KBaTeBiO_6$ solution. The higher annealing temperature for the second solution is required to remove the binders. The $KBaTeBiO_6$-coated TiO_2/FTO electrode acts as a working electrode and a Pt electrode was used as the counter electrode. The two electrodes were then sandwiched together with 25 μm thick thermoplastic Surlyn film and the iodide/triiodide electrolyte (iodolyte AN-50, Solaronix) was injected between the electrodes through a predrilled hole on the Pt electrode (Solaronix, Australia), which is made from screen-printing a Plastisol T/SP precursor on the FTO substrate. The active area of the cells was 0.25 cm^2. All the devices were tested under the standard AM1.5 solar illumination conditions. The entire device fabrication and testing were performed under ambient humid conditions (30−50% relative humidity). No glovebox was used during material synthesis and device testing.

■ RESULTS AND DISCUSSION

An ideal double perovskite with a general formula of $A'A''B'B''X_6$ is an extension of the cubic ABX_3 perovskite structure, where A′ and A″ represent inequivalent A-site cations while B′ and B″ represent inequivalent B-site cations. The B-site cations are octahedrally (6-coordinated) coordinated by the X-site anions, while the A-site cations occupy the cube-octahedral (12-coordinated) voids generated within the rigid, corner-connected BX_6 octahedral network, as shown in Figure 1a. For a fixed anion X, the perovskite structure can accommodate a varied range of cations both at the A- and B-sites.[35] This flexibility arises from the ability of the BX_6 octahedra to undergo cooperative tiltings[36] that optimize the coordination environment of the cations. In our search for

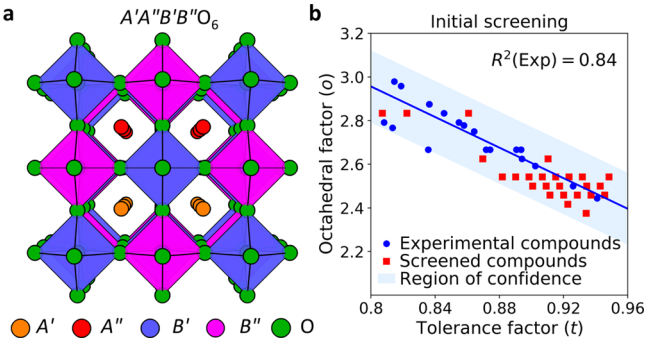

Figure 1. (a) Structure of an ideal double perovskite having layered ordering at the A-site and rock-salt ordering at the B-site. (b) Variation of the octahedral factor with the tolerance factor for previously synthesized $A'A''B'BiO_6$ (from ICSD) and for the screened hypothetical compounds conforming to the experimental trend line within the region of confidence.

inorganic oxide double perovskites that can mimic lead-halide perovskites, we fixed at least one of the B-sites to be a Bi^{3+} cation. The use of O^{2-} anions opens a large combinatorial space of cations to occupy the remaining A- and B-sites. We included cations with atomic number less than Bi as possible candidates. We excluded lanthanides and radioactive Tc as possible choices and included all possible oxidation states for multivalent cations. From a simple charge balance, there are 29,515 unique $A'A''B'BiO_6$ double perovskite oxides.

The next step was to screen potential candidates for DFT calculations. We devised a screening criterion based on the structural parameters of the 28 unique $A'A''B'BiO_6$ double perovskites that have been previously synthesized and were listed in ICSD.[27] It should be noted that instead of the 1:1:1:1 ratio of A′, A″, B′, and B″, many entries in ICSD include compounds with varying composition ratios; however, we only used one combination with the composition ratio closest to 1:1:1:1. We used the modified tolerance factor[37] ($t = (rA + rX/\sqrt{2}(rB + rX))$ and the octahedral factor ($o = rB/rX$), where r_A, r_B, and r_X are the weighted average radii of A-, B-, and X-site ions, respectively, that have been shown to predict the formability in perovskites.[38−40] We used Slater's empirical atomic radii,[41] instead of Shannon's ionic radii[42] used in conventional definitions[37] of o and t, as the former is independent of the coordination environment and oxidation state of an element, which are unknown for a hypothetical perovskite. We find that our simple two-parameter linear regression model—built on o and t structural parameters alone—can accurately describe the formability of all previously known Bi-based double perovskite oxides (reported in ICSD) with an R-squared value of 0.84, as shown in Figure 1b. We used the farthest lying experimental data point (blue) from the fitted line to define a rectangular area and use it as the region of confidence. We find a total of 144 hypothetical $A'A''B'BiO_6$ double perovskites lying within this region of confidence as shown using red data points in Figure 1b for subsequent geometry optimization. Many of the screened compounds have the same set of o and t values and are overlying in Figure 1b.

For the 144 screened $A'A''B'BiO_6$ double perovskites, we carried out DFT-based geometry optimization in a two-step procedure involving a coarse relaxation followed by a fine relaxation (see the details in the Methods section). For the coarse relaxation, we considered all the hypothetical compounds to be ideal double perovskites without any

DOI: 10.1021/acs.chemmater.9b01025
Chem. Mater. 2019, 31, 4769−4778

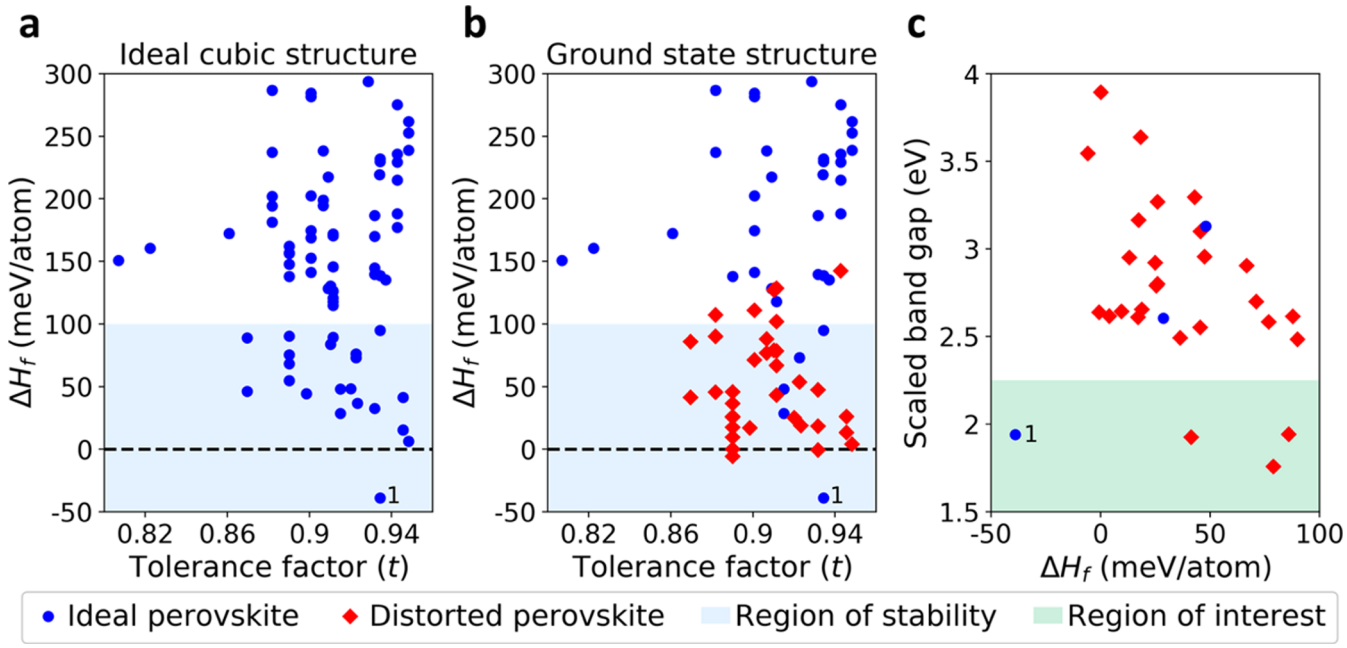

Figure 2. Variation of formation enthalpy (ΔH_f) with tolerance factor for A′A″B′BiO_6 compounds with (a) cubic double perovskite structure and (b) ground-state structure with octahedral rotations. (c) Variation of the scaled HSE06 + SOC band gap with formation enthalpy for the ground-state structures of stable A′A″B′BiO_6 compounds. The compounds with formation enthalpy lower than 100 meV/atom are considered formable. The marker 1 in (a−c) corresponds to $KBaTeBiO_6$.

octahedral tilts. An ideal double perovskite can be classified into one of two space-group symmetries: $Fm\bar{3}m$ for A′ = A″ and $P4/nmm$ for A′ ≠ A″. As shown in Figure 1a, we imposed layered ordering for the A-site cations (A′ and A″) and rock-salt ordering for the B-site cations (B′ and B″), which are most prevalent in ordered double perovskites.[43] We used the same DFT settings as those used in the OQMD[32,44] to enable the calculation of formation enthalpy (ΔH_f) of the hypothetical double perovskites with respect to the most stable reactants, which can be elements or compounds (described in Supporting Information). In principle, a negative-formation enthalpy suggests that a compound is stable and can be synthesized. However, Sun et al.[45] have recently shown that metastable compounds are fairly common, as they report that about 90th percentile of the experimental binary oxides lie within 94 meV/atom above the ground-state polymorph. Thus, we set a similar criterion to also include metastable A′A″B′BiO_6 compounds having ΔH_f < 100 meV/atom that can be expected to be formable. Figure 2a shows the variation of formation enthalpy with tolerance factor for all the screened ideal double perovskites. Within the ideal double perovskite structure, as shown in Figure 2a, only one compound has a negative formation enthalpy: $KBaTeBiO_6$ (ΔH_f = −39 meV/atom) and 21 compounds lie inside the region of formability (ΔH_f < 100 meV/atom).

As mentioned previously, cooperative tilting of the BX_6 octahedra[36] can further stabilize the perovskite structure by lowering the crystal symmetry. The octahedral tilts and their effects on the space-group symmetry have been studied extensively for the double perovskite structure[46−48] and are summarized in Supporting Information (Table S1). For those compounds having ΔH_f < 200 meV/atom, we performed geometry optimization starting from all possible octahedral tilt patterns. We find that, for most of the compounds, the ground state has octahedral tilts. As shown in Figure 2b, there are now 36 compounds in the region of formability (ΔH_f < 100 meV/atom) with 5 compounds having a negative formation enthalpy: $KBaTeBiO_6$, $SrBaVBiO_6$, $RbYVBiO_6$, $CsPbMoBiO_6$, and $RbYNbBiO_6$. Of the 36 formable compounds, there are 5 compounds that have the ideal perovskite structure as their ground state.

Any potential candidate for photovoltaic applications, in addition to being formable, should also exhibit an optimal band gap (∼1.6 eV) and electronic structure for maximum possible absorption of the solar spectrum. GGA functionals, such as the PBE functional,[30] are known to underestimate the band gap. To predict experimental band gaps more accurately, we employed the HSE06 functional.[49,50] We also included spin−orbit coupling effects (SOC), as they are expected to be significant because of the presence of the heavy Bi^{3+} cation. However, as HSE06 + SOC calculations are computationally expensive, we used them to calculate the band gap of 25% of the formable compounds. For the remaining formable compounds, we linearly scaled their PBE band gaps (E_g(PBE)) using E_g(HSE06 + SOC) = 0.87E_g(PBE) + 0.84, to obtain scaled HSE06 + SOC band gaps (E_g(HSE06 + SOC)). Such empirical linear scaling has previously been shown to have a reasonable accuracy for predicting calculated GW band gaps.[51] We show the scaled band gap of the compounds that are below our formability criteria (ΔH_f < 100 meV/atom) in Figure 2c. We find only five compounds in their most stable phase having an intermediate E_g < 2.25 eV. Only two of these compounds are lead-free. These two compounds are $KBaTeBiO_6$ and $SrBaVBiO_6$ that have a calculated E_g of 1.94 and a scaled E_g of 2.18 eV, respectively.

In addition to an optimal band gap, highly dispersed conduction and valence bands are desirable for faster transport of electrons and holes. Based on the calculated band structure, we find that $SrBaVBiO_6$ has flat bands, as shown in Supporting Information (see Figure S1). However, $KBaTeBiO_6$ has widely

DOI: 10.1021/acs.chemmater.9b01025
Chem. Mater. 2019, 31, 4769−4778

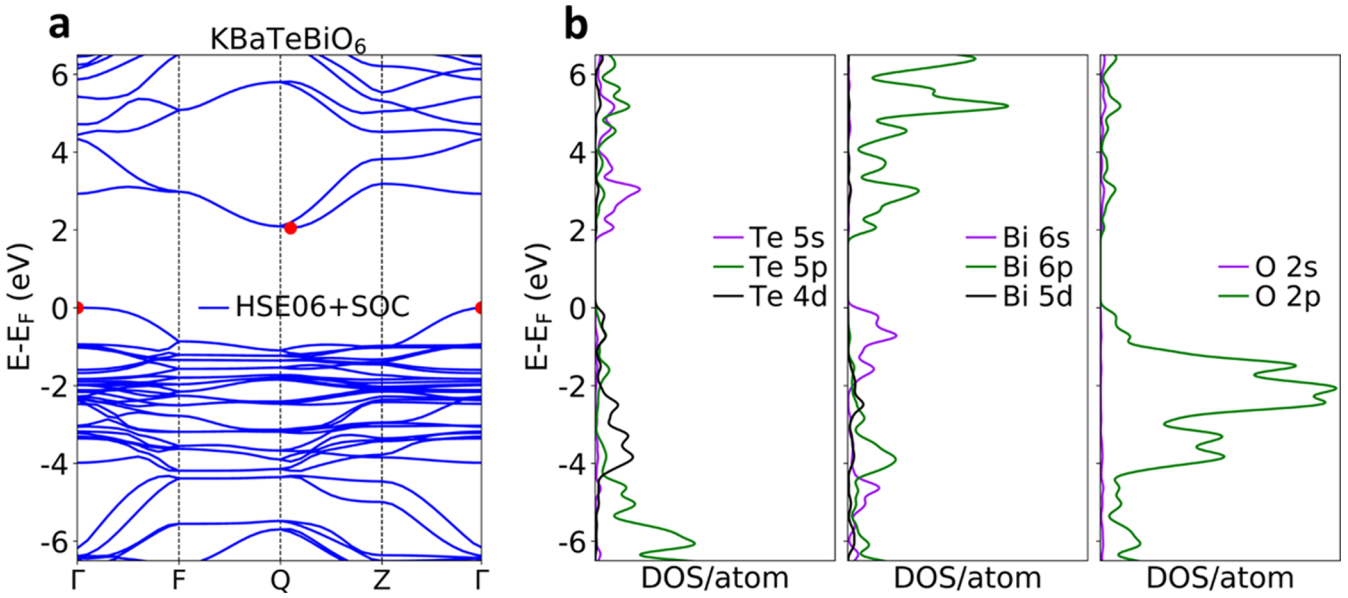

Figure 3. (a) Calculated band structure and (b) atom-projected density of states (DOS/atom) for $KBaTeBiO_6$ obtained using the HSE06 functional with spin−orbit coupling.

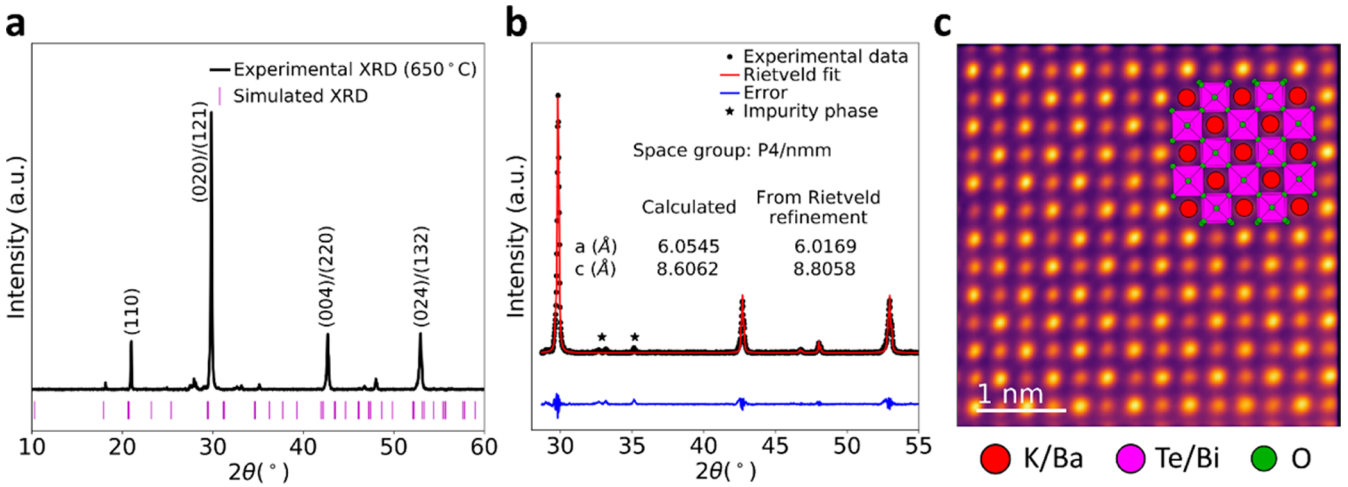

Figure 4. (a) Experimental XRD pattern for $KBaTeBiO_6$ annealed at 650 °C and the simulated XRD pattern of the DFT-optimized structure. (b) Rietveld refinement of the experimental XRD data and the quality of the fit. (c) Atomic resolution STEM−HAADF image of the $KBaTeBiO_6$ powder sample with an overlaid atomic model.

dispersed bands, as shown in the band structure plot calculated using HSE06 + SOC (Figure 3a). The atom-projected DOS is shown in Figure 3b. $KBaTeBiO_6$ has a predicted indirect band gap of 1.94 eV from Γ (0, 0, 0) to (0, 0.45, 0.5), which is similar to the calculated indirect band gap of 2.06 eV (2.62 eV) for $Cs_2AgBiBr_6$ ($Cs_2AgBiCl_6$).[22] The theoretical direct band gap of $KBaTeBiO_6$ is 2.83 eV and occurs at Γ, whereas the direct band gap of $Cs_2AgBiBr_6$ ($Cs_2AgBiCl_6$) is 2.45 eV (3 eV). The effective mass of holes in $KBaTeBiO_6$ is $0.25m_e$ (m_e is the rest mass of an electron) along Γ−Z, which is heavier than that for $Cs_2AgBiBr_6$ ($0.14m_e$) and $Cs_2AgBiCl_6$ ($0.15m_e$), whereas the effective mass of electrons for $KBaTeBiO_6$ is $0.28m_e$ along the conduction band minimum (0, 0.45, 0.5) to Q (0, 0.5, 0.5), which is lighter than that of $Cs_2AgBiBr_6$ ($0.37m_e$) and $Cs_2AgBiCl_6$ ($0.53m_e$). Overall, the low effective masses of electrons and holes for $KBaTeBiO_6$ points toward a favorable carrier transport.

As shown in the DOS plot of $KBaTeBiO_6$ in Figure 3b, the valence band is predominantly made up of O 2p and Bi 6s states with a small contribution of Te 4d states. The conduction band is largely made up of Bi 6p and Te 5s states with a small contribution from O 2p states. As the Bi 6s antibonding states are present at the valence band edge, rather than the conduction band edge, it implies that Bi is in +3 oxidation state, and it can be expected to impart the defect tolerance due to the lone-pair chemistry as discussed earlier.[52] Furthermore, we find 2.73*e* in the empty conduction-band states of Bi, which supports a +3 oxidation state for Bi. We have described the chemical bonding of $KBaTeBiO_6$ in detail in Supporting Information (see Figure S3). Moreover, a comparison of the calculated absorption spectra of $KBaTeBiO_6$ and $Cs_2AgBiBr_6$ (as shown in Figure S2) shows promising absorbance for the former.

To validate our theoretical predictions, we have synthesized $KBaTeBiO_6$ using a wet-chemistry method (see Methods). We

DOI: 10.1021/acs.chemmater.9b01025
Chem. Mater. 2019, 31, 4769−4778

find that, annealing at 650 °C is necessary to obtain high phase purity. Figure 4a shows the X-ray diffraction (XRD) pattern of the samples synthesized at 650 °C and the simulated XRD pattern of DFT-optimized $KBaTeBiO_6$ unit cell. We chose the annealing temperature based on the thermogravimetric analysis on the mixed precursors (as shown in Figure S4). The sample annealed at 650 °C shows major diffraction peaks at 21.02°, 29.86°, 42.87°, and 53.02° that correspond to (110), convoluted (020)/(112), (004)/(220), and (024)/(132) planes, respectively. Rietveld refinements of the experimental XRD data are provided in Figure 4b. As calculated from DFT, the ground state of $KBaTeBiO_6$ belongs to the *P*4/*nmm* space group. The calculated lattice parameters from DFT ($a = b =$ 6.0545 Å, c = 8.6062 Å) are within 2.3% of the experimental lattice parameters ($a = b =$ 6.0169 Å, c = 8.8058 Å), as obtained from Rietveld refinement. The refined atomic positions are provided in Table 1.

Table 1. Atomic Positions for $KBaTeBiO_6$ Obtained after Rietveld Refinement

element	wycoff site	*x*	*y*	*z*
K	2a	0.75	0.25	0.0
Ba	2b	0.75	0.25	0.5
Te	2c	0.25	0.25	0.25529
Bi	2c	0.25	0.25	0.76577
O	8j	0.47965	0.47965	0.2638
O	2c	0.25	0.25	0.02919
O	2c	0.25	0.25	0.48639

To investigate the stability of the material, we stored the samples under ambient conditions and performed XRD after 380 days (Supporting Information Figure S5). We did not observe any apparent changes in the XRD of the sample, which points toward the excellent stability of $KBaTeBiO_6$. To map the chemical composition of the synthesized powder, we have performed EDS using STEM, which confirms the presence of all the five elements. The elemental chemical maps along with their integrated spectrum are shown in Figure S6. To estimate the variability in cation stoichiometry, we have acquired multiple EDS datasets, the findings of which are summarized in Table S2. Instead of an expected 1:1:1:1 cation ratio of K/Ba/Te/Bi, we obtain an average ratio of 0.45 (±0.028):1.32 (±0.123):1.05 (±0.049):1.18 (±0.157). The composition is normalized such that the total composition of all cations is 4 per formula unit, as in $KBaTeBiO_6$. The lower ratio of K could either be because of the presence of K vacancies or excess Te and Bi cations occupying the A-site. Further optimization of the synthesis process to control the stoichiometry along with the role of nonstoichiometry on the optoelectronic properties will be the subject of future studies.

To further confirm the formation of the perovskite structure, we have performed atomic-resolution imaging of the synthesized $KBaTeBiO_6$ particles using aberration-corrected STEM. Figure 4c shows an atomic resolution HAADF image of the $KBaTeBiO_6$ lattice along the (001) projection with part of the image overlaid with an atomic model of $KBaTeBiO_6$. In HAADF imaging mode, the intensity of every pixel is approximately proportional to the squared atomic number ($\sim Z^2$) of the atomic column.[53] As a result, the B-site atomic columns containing Te (Z = 52) and Bi (Z = 83) appear the brightest while A-site atomic columns containing K (Z = 19) and Ba (Z = 56) appear dimmer. The average in-plane lattice parameters obtained from the HAADF image ($a = b =$ 6.0045 Å) compare well with those obtained from DFT and XRD. A detailed analysis of intensity profiles in the atomic resolution HAADF image along with atomic-scale chemical composition mapping using electron energy loss spectroscopy (EELS) is provided in the (Supporting Information, Figures S7 and S8).

After confirming the formation of a perovskite structure, we focus on the optical properties of $KBaTeBiO_6$. To determine the experimental optical gap of $KBaTeBiO_6$, we measured the absorption spectrum of $KBaTeBiO_6$ (thin film on a glass slide) using a UV−vis spectrophotometer. The absorption spectrum,

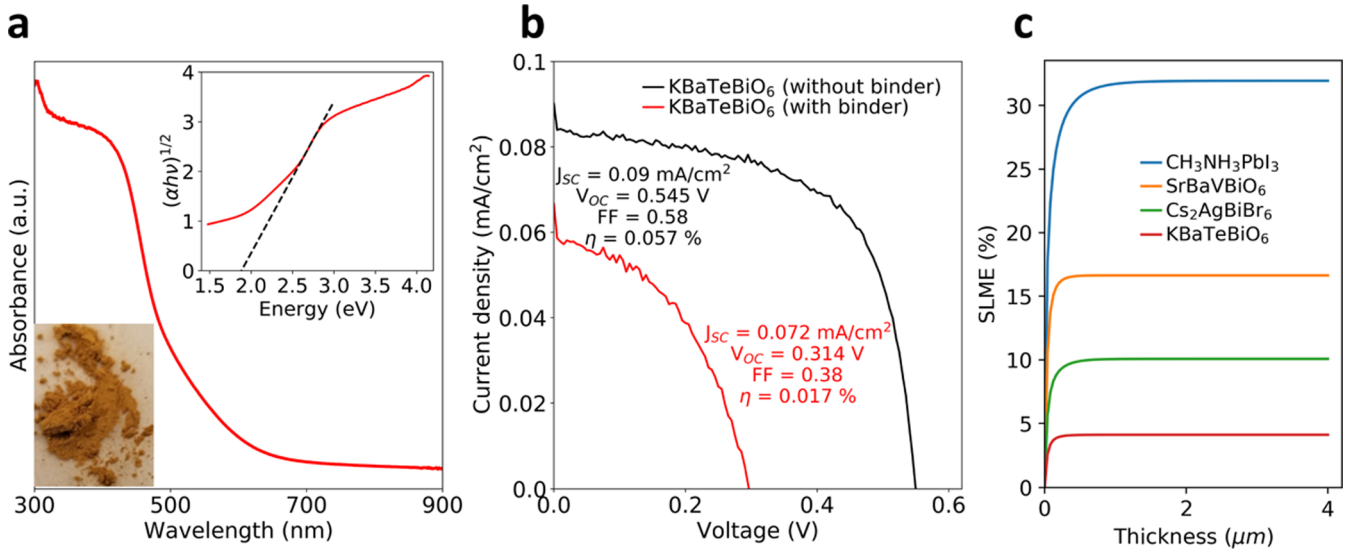

Figure 5. (a) Absorption spectrum of the $KBaTeBiO_6$ film measured using a UV−vis spectrophotometer. The inset shows a Tauc plot with an estimated indirect band gap of 1.88 eV. The bottom left corner of (a) shows the image of the as-synthesized $KBaTeBiO_6$ powder. (b) J−V characteristics of the most efficient $KBaTeBiO_6$ PEC solar cell fabricated without (red) and with a binder (black). (c) Comparison of variation of calculated spectroscopic limited maximum efficiencies for $KBaTeBiO_6$, $SrBaVBiO_6$, prototype lead-halide perovskite, and bismuth-halide double perovskite.

DOI: 10.1021/acs.chemmater.9b01025
Chem. Mater. 2019, 31, 4769−4778

as shown in Figure 5a, shows a major onset near 520 nm. The major onset in the measured absorption spectrum is not very sharp, which can be attributed to the indirect band gap as predicted by DFT. We used the Tauc method (shown in the inset of Figure 5a): $(\alpha h\nu)^{1/2}$ versus $h\nu$; α being the absorption coefficient; to estimate the indirect band gap of $KBaTeBiO_6$ to be 1.88 eV. As mentioned earlier, the synthesized $KBaTeBiO_6$ powder exhibits cation nonstoichiometry (deviation from 1:1:1:1 cation ratio), which could have important implications on the material stability and electronic structure. For instance, preliminary DFT calculations at the PBE level show a band gap reduction of 1.18 eV for $K_{0.625}Ba_{1.375}Te_{0.875}Bi_{1.125}O_6$ as compared to $KBaTeBiO_6$, without introducing any defect states (see Figure S9). $K_{0.625}Ba_{1.375}Te_{0.875}Bi_{1.125}O_6$ has a $P\bar{1}$ ground-state structure corresponding to a tilt pattern of $a^-b^-c^-$ with a calculated ΔH_f of −148 meV/atom. The lower ΔH_f of $K_{0.625}Ba_{1.375}Te_{0.875}Bi_{1.125}O_6$ than $KBaTeBiO_6$ suggests that the cation nonstoichiometry is thermodynamically favorable. Further investigation on the role of nonstoichiometry, defects, and disorder will be the subject of a future study; however, these preliminary DFT results suggest nonstoichiometry to be an effective route to control the electronic structure.

To demonstrate the applicability of $KBaTeBiO_6$ as an active absorber layer in solar cells, we have fabricated regenerative PEC solar cells. The device architecture (see Figure S10) is FTO/TiO_2/$KBaTeBiO_6$/iodide-triiodide/Pt. Two types of devices were fabricated based on the solution preparation of $KBaTeBiO_6$, one without any binders in the $KBaTeBiO_6$ solution and another with binders for better adhesion of the perovskite particles together as well as with TiO_2 nanoparticles. More details on the solution preparation method can be found in the experimental section. Figure 5b shows the current density (J) versus voltage (V) characteristics of the best devices for both cases. The photovoltaic parameters for all the fabricated devices are reported in the Supporting Information (Table S3). The devices without binders show superior performance than those with binders possibly because of efficient electron transport from the absorber layer to TiO_2. The average efficiency obtained for these first-generation devices without binders is 0.038 ± 0.012% and for the devices with binders is 0.011 ± 0.007%. The highest achieved efficiency of the best device without binders is 0.057%. Compared to other bismuth-based perovskite solar cells that have been reported so far, such as $Cs_2AgBiBr_6$[54] (η = 1.04%, E_g = 2.04 eV), $Cs_3Bi_2I_9$[55] (η = 1.09%, E_g = 2.20 eV), and $CH_3NH_3Bi_2I_9$[55] (η = 0.12%, E_g = 2.10 eV), the efficiency for the best $KBaTeBiO_6$ device is low. However, $KBaTeBiO_6$ shows far better material stability than bismuth-based halide perovskites. Furthermore, solar cells using $KBaTeBiO_6$ nanoparticles show similar performance to those based on high-quality thin films of other inorganic oxide perovskites (summarized in Supporting Information Table S4).

To predict the theoretical efficiency of $KBaTeBiO_6$ that could be achieved by improvements in device fabrication and material optimization, we have calculated its spectroscopic limited maximum efficiency (SLME)[56] and compared it to cubic-phase $CH_3NH_3PbI_3$, $Cs_2AgBiBr_6$, and $SrBaVBiO_6$. We have used the standard AM1.5G solar spectrum at 25 °C for the SLME calculations.[57] Figure 5c shows the comparison of SLME for the four compounds. The exchange−correlation functionals used for calculating the absorption spectra for $CH_3NH_3PbI_3$ and $Cs_2AgBiBr_6$ are PBEsol and HSE06 + SOC, respectively. These functionals have been chosen as they show the closest agreement to the experimental band gap for respective material systems. For $KBaTeBiO_6$, we have calculated the absorption spectra using HSE06 + SOC. For $SrBaVBiO_6$, we have calculated the absorption spectra using PBE + SOC and scaled the band gap from 1.52 to 2.18 eV (scaled HSE06 + SOC band gap) using a scissors operator. SLME is a comprehensive predictive metric, which accounts for the difference between the indirect and direct band gaps, the strength of absorption and nonradiative recombination losses to predict the theoretical efficiency of a material. The prototype lead-halide perovskite $CH_3NH_3PbI_3$ has an extremely high predicted SLME of 31.69% for a 1 μm thick film, which is due to the sharp absorption onset resulting from a direct band gap. For $Cs_2AgBiBr_6$, its indirect band gap and a difference of about ∼0.5 eV between the indirect band gap and the next allowed direct transition results in an SLME of 10.06% for a 1 μm thick film. In comparison, the calculated SLME of 1 μm thick films of $KBaTeBiO_6$ is 4.11%. It should be noted that SLME is strongly dependent on the band gap of the material. As mentioned earlier (Figure S9), our preliminary theoretical results suggest that the band gap of $KBaTeBiO_6$ may be tuned by changing the cation stoichiometry, which may lead to even higher SLME. For $SrBaVBiO_6$, which has indirect and direct band gaps of 2.18 and 2.25 eV, respectively, we find a larger SLME of 16.64% for a 1 μm thick film. While this suggests higher absorbance of the incoming photons in $SrBaVBiO_6$, its high effective mass of holes ($0.7m_e$) and electrons ($2.11m_e$), is expected to result in less efficient carrier separation, and potentially lower cell efficiency.

Finally, we briefly discuss various strategies that can lead to improvements in the efficiency of the $KBaTeBiO_6$-based solar cells. As we have discussed before, the stoichiometry of the cations has a large impact on the band gap without resulting in defect levels. Hence, control and optimization of the stoichiometry will be an important parameter to achieve higher efficiency. Likewise, control over the oxygen stoichiometry will be another important parameter as oxygen vacancies can either act as shallow donors or lead to deep level defects as observed in wide-band gap semiconductors, such as in ZnO.[58] Another approach could be the growth of high-quality thin films—such as using aerosol-based techniques[59]—to avoid grain boundaries, which under certain conditions can act as recombination centers in perovskites.[14] Finally, for the PEC-based solar cells, using a compact layer of TiO_2, as used in solid-state dye-sensitized solar cells, would prevent charge recombination of the excited carriers in the FTO electrode with the oxidized species in the electrolyte.[60]

■ CONCLUSIONS

In summary, using a linear regression analysis and high-throughput DFT calculations, we have predicted a stable Bi-based double perovskite oxide, $KBaTeBiO_6$ from a vast composition space of thousands of compounds which is similar to the prototype halide double perovskites $Cs_2AgBiBr_6$ and $Cs_2AgBiCl_6$. We have successfully synthesized $KBaTeBiO_6$, which crystallizes into a double perovskite structure with excellent stability under ambient conditions. The experimentally measured indirect band gap of $KBaTeBiO_6$ is 1.88 eV, which is similar to the band gap of prototype halide double perovskites $Cs_2AgBiBr_6$ and $Cs_2AgBiCl_6$. In addition to a favorable band gap, $KBaTeBiO_6$ has comparable effective masses of charge carriers to prototype lead-halide perovskites and bismuth-halide double perovskites. The best performing

DOI: 10.1021/acs.chemmater.9b01025
Chem. Mater. 2019, 31, 4769−4778

$KBaTeBiO_6$ nanoparticles-based regenerative PEC solar cell shows an efficiency of 0.057%. Moreover, preliminary DFT calculations reveal significant electronic structure tunability by varying the cation stoichiometry within the $KBaTeBiO_6$ material system.

In future, the study and control of defects including cation nonstoichiometry and disorder in $KBaTeBiO_6$ will be a crucial task to achieve optimal performance from these semiconductors. More advanced synthesis techniques, such as aerosol routes guided by defect calculation and atomic-scale STEM characterization, will allow us to accomplish this goal. Our study opens up a large and hitherto unexplored composition space for identifying promising defect-tolerant semiconductors materials for a variety of optoelectronic applications.

■ ASSOCIATED CONTENT

Supporting Information

The Supporting Information is available free of charge on the ACS Publications website at DOI: 10.1021/acs.chemmater.9b01025.

Calculation of formation enthalpy; octahedral tilts in double perovskites; electronic structure of $SrBaVBiO_6$; chemical bonding analysis for $KBaTeBiO_6$; calculated absorption spectra for $KBaTeBiO_6$; thermogravimetric analysis; stability of as-synthesized $KBaTeBiO_6$ powder; STEM−EDS analysis; STEM−EELS analysis; effect of nonstoichiometry on the electronic structure; device architecture and performance; and perovskite oxide-based photovoltaic devices (PDF)

CIF files of DFT-optimized and Rietveld-refined structures (ZIP)

■ AUTHOR INFORMATION

Corresponding Author

*E-mail: rmishra@wustl.edu.

ORCID

Hemant Kumar Mulmudi: 0000-0002-9722-9877

Albina Y. Borisevich: 0000-0002-3953-8460

Rohan Mishra: 0000-0003-1261-0087

Present Address

¶(S.B.C.) Virtual Engineering Center, Korea Institute of Ceramic Engineering and Technology, Jinju 52851, Republic of Korea.

Author Contributions

R.M. conceived and coordinated the project. A.S.T., S.B.C., G.P., and R.M. performed the DFT calculations and analysis. S.K., L-Y.L., M.K. and R.W. carried out the synthesis, experimental characterization and device fabrication under the supervision of P.B. A.S.T., K.A.U, A.Y.B., and R.M. carried out the STEM experiments. A.S.T. and R.M. wrote the paper with contributions from other coauthors. All authors discussed and commented on the manuscript.

Notes

The authors declare no competing financial interest.

■ ACKNOWLEDGMENTS

This work was supported by the National Science Foundation (NSF) grant number 1806147. This work used computational resources of the Extreme Science and Engineering Discovery Environment (XSEDE), which is supported by NSF grants ACI-1053575 and ACI-1548562. R.M. acknowledges partial support through Ralph E. Power Junior Faculty Enhancement Award from Oak Ridge Associated Universities. G.P. acknowledges support from the Los Alamos National Laboratory's Laboratory Directed Research and Development (LDRD) program (20190043DR) and computational support from Los Alamos National Laboratory's high performance computing clusters. A.Y.B. was supported by the Division of Materials Science and Engineering, United States Department of Energy. Microscopy performed as part of a user project at the Center for Nanophase Materials Sciences (CNMS), which is sponsored by the Scientific User Facilities Division, Office of Basic Energy Sciences, United States Department of Energy. H.K.M. acknowledges funding received from the Australian Renewable Energy Agency (ARENA) to implement this project.

■ REFERENCES

(1) Kojima, A.; Teshima, K.; Shirai, Y.; Miyasaka, T. Organometal Halide Perovskites as Visible-Light Sensitizers for Photovoltaic Cells. *J. Am. Chem. Soc.* **2009**, *131*, 6050−6051.

(2) Green, M. A.; Hishikawa, Y.; Dunlop, E. D.; Levi, D. H.; Hohl-Ebinger, J.; Ho-Baillie, A. W. Y. Solar cell efficiency tables (version 52). *Prog. Photovoltaics Res. Appl.* **2018**, *26*, 427−436.

(3) Zhao, X.; Park, N.-G. Stability Issues on Perovskite Solar Cells. *Photonics* **2015**, *2*, 1139−1151.

(4) Leijtens, T.; Eperon, G. E.; Pathak, S.; Abate, A.; Lee, M. M.; Snaith, H. J. Overcoming ultraviolet light instability of sensitized TiO_2 with meso-superstructured organometal tri-halide perovskite solar cells. *Nat. Commun.* **2013**, *4*, 2885.

(5) Nagabhushana, G. P.; Shivaramaiah, R.; Navrotsky, A. Direct calorimetric verification of thermodynamic instability of lead halide hybrid perovskites. *Proc. Natl. Acad. Sci. U.S.A.* **2016**, *113*, 7717−7721.

(6) Kavadiya, S.; Niedzwiedzki, D. M.; Huang, S.; Biswas, P. Electrospray-Assisted Fabrication of Moisture-Resistant and Highly Stable Perovskite Solar Cells at Ambient Conditions. *Adv. Energy Mater.* **2017**, *7*, 1700210.

(7) Babayigit, A.; Ethirajan, A.; Muller, M.; Conings, B. Toxicity of organometal halide perovskite solar cells. *Nat. Mater.* **2016**, *15*, 247−251.

(8) Stoumpos, C. C.; Malliakas, C. D.; Kanatzidis, M. G. Semiconducting tin and lead iodide perovskites with organic cations: phase transitions, high mobilities, and near-infrared photoluminescent properties. *Inorg. Chem.* **2013**, *52*, 9019−9038.

(9) Stoumpos, C. C.; Frazer, L.; Clark, D. J.; Kim, Y. S.; Rhim, S. H.; Freeman, A. J.; Ketterson, J. B.; Jang, J. I.; Kanatzidis, M. G. Hybrid germanium iodide perovskite semiconductors: active lone pairs, structural distortions, direct and indirect energy gaps, and strong nonlinear optical properties. *J. Am. Chem. Soc.* **2015**, *137*, 6804−6819.

(10) Yin, W.-J.; Yang, J.-H.; Kang, J.; Yan, Y.; Wei, S.-H. Halide perovskite materials for solar cells: a theoretical review. *J. Mater. Chem. A* **2015**, *3*, 8926−8942.

(11) Yin, W.-J.; Shi, T.; Yan, Y. Unusual defect physics in $CH_3NH_3PbI_3$ perovskite solar cell absorber. *Appl. Phys. Lett.* **2014**, *104*, 063903.

(12) Du, M. H. Efficient carrier transport in halide perovskites: theoretical perspectives. *J. Mater. Chem. A* **2014**, *2*, 9091−9098.

(13) Yin, W.-J.; Shi, T.; Yan, Y. Unique properties of halide perovskites as possible origins of the superior solar cell performance. *Adv. Mater.* **2014**, *26*, 4653−4658.

(14) Thind, A. S.; Luo, G.; Hachtel, J. A.; Morrell, M. V.; Cho, S. B.; Borisevich, A. Y.; Idrobo, J. C.; Xing, Y.; Mishra, R. Atomic Structure and Electrical Activity of Grain Boundaries and Ruddlesden-Popper Faults in Cesium Lead Bromide Perovskite. *Adv. Mater.* **2019**, *31*, No. e1805047.

DOI: 10.1021/acs.chemmater.9b01025
Chem. Mater. 2019, 31, 4769−4778

(15) Morrell, M. V.; He, X.; Luo, G.; Thind, A. S.; White, T. A.; Hachtel, J. A.; Borisevich, A. Y.; Idrobo, J.-C.; Mishra, R.; Xing, Y. Significantly Enhanced Emission Stability of $CsPbBr_3$ Nanocrystals via Chemically Induced Fusion Growth for Optoelectronic Devices. *ACS Appl. Nano Mater.* **2018**, *1*, 6091−6098.
(16) Xiao, Z.; Meng, W.; Wang, J.; Mitzi, D. B.; Yan, Y. Searching for promising new perovskite-based photovoltaic absorbers: the importance of electronic dimensionality. *Mater. Horiz.* **2017**, *4*, 206−216.
(17) Huang, X.; Huang, S.; Biswas, P.; Mishra, R. Band Gap Insensitivity to Large Chemical Pressures in Ternary Bismuth Iodides for Photovoltaic Applications. *J. Phys. Chem. C* **2016**, *120*, 28924−28932.
(18) Cho, S. B.; Gazquez, J.; Huang, X.; Myung, Y.; Banerjee, P.; Mishra, R. Intrinsic point defects and intergrowths in layered bismuth triiodide. *Phys. Rev. Mater.* **2018**, *2*, 064602.
(19) Thind, A. S.; Huang, X.; Sun, J.; Mishra, R. First-Principles Prediction of a Stable Hexagonal Phase of $CH_3NH_3PbI_3$. *Chem. Mater.* **2017**, *29*, 6003−6011.
(20) Volonakis, G.; Filip, M. R.; Haghighirad, A. A.; Sakai, N.; Wenger, B.; Snaith, H. J.; Giustino, F. Lead-Free Halide Double Perovskites via Heterovalent Substitution of Noble Metals. *J. Phys. Chem. Lett.* **2016**, *7*, 1254−1259.
(21) Slavney, A. H.; Hu, T.; Lindenberg, A. M.; Karunadasa, H. I. A Bismuth-Halide Double Perovskite with Long Carrier Recombination Lifetime for Photovoltaic Applications. *J. Am. Chem. Soc.* **2016**, *138*, 2138−2141.
(22) McClure, E. T.; Ball, M. R.; Windl, W.; Woodward, P. M. Cs_2AgBiX_6(X = Br, Cl): New Visible Light Absorbing, Lead-Free Halide Perovskite Semiconductors. *Chem. Mater.* **2016**, *28*, 1348−1354.
(23) Filip, M. R.; Hillman, S.; Haghighirad, A. A.; Snaith, H. J.; Giustino, F. Band Gaps of the Lead-Free Halide Double Perovskites $Cs_2BiAgCl_6$ and $Cs_2BiAgBr_6$ from Theory and Experiment. *J. Phys. Chem. Lett.* **2016**, *7*, 2579−2585.
(24) Wei, F.; Deng, Z.; Sun, S.; Zhang, F.; Evans, D. M.; Kieslich, G.; Tominaka, S.; Carpenter, M. A.; Zhang, J.; Bristowe, P. D.; Cheetham, A. K. Synthesis and Properties of a Lead-Free Hybrid Double Perovskite: $(CH_3NH_3)_2AgBiBr_6$. *Chem. Mater.* **2017**, *29*, 1089−1094.
(25) Grinberg, I.; West, D. V.; Torres, M.; Gou, G.; Stein, D. M.; Wu, L.; Chen, G.; Gallo, E. M.; Akbashev, A. R.; Davies, P. K.; Spanier, J. E.; Rappe, A. M. Perovskite oxides for visible-light-absorbing ferroelectric and photovoltaic materials. *Nature* **2013**, *503*, 509−512.
(26) Kim, T. W.; Hur, S. G.; Hwang, S.-J.; Park, H.; Park, Y.; Choi, W.; Choy, J.-H. Substitution effect of pentavalent bismuth ions on the electronic structure and physicochemical properties of perovskite-structured $Ba(In_{0.5}Ta_{0.5-x}Bi_x)O_3$ semiconductors. *Mater. Res. Bull.* **2007**, *42*, 1914−1920.
(27) Inorganic Crystal Structure Database. https://icsd.fiz-karlsruhe.de (Accessed on June 15, 2017).
(28) Kresse, G.; Furthmüller, J. Efficient iterative schemes for ab initio total-energy calculations using a plane-wave basis set. *Phys. Rev. B: Condens. Matter Mater. Phys.* **1996**, *54*, 11169−11186.
(29) Blöchl, P. E. Projector augmented-wave method. *Phys. Rev. B: Condens. Matter Mater. Phys.* **1994**, *50*, 17953.
(30) Perdew, J. P.; Burke, K.; Ernzerhof, M. Generalized gradient approximation made simple. *Phys. Rev. Lett.* **1996**, *77*, 3865−3868.
(31) Monkhorst, H. J.; Pack, J. D. Special points for Brillouin-zone integrations. *Phys. Rev. B* **1976**, *13*, 5188−5192.
(32) Kirklin, S.; Saal, J. E.; Meredig, B.; Thompson, A.; Doak, J. W.; Aykol, M.; Rühl, S.; Wolverton, C. The Open Quantum Materials Database (OQMD): assessing the accuracy of DFT formation energies. *npj Comput. Mater.* **2015**, *1*, 15010.
(33) Sheikh, M. S.; Ghosh, D.; Dutta, A.; Bhattacharyya, S.; Sinha, T. Lead free double perovskite oxides Ln_2NiMnO_6 (Ln= La, Eu, Dy, Lu), a new promising material for photovoltaic application. *Mater. Sci. Eng., B* **2017**, *226*, 10−17.
(34) Ito, S.; Chen, P.; Comte, P.; Nazeeruddin, M. K.; Liska, P.; Péchy, P.; Grätzel, M. Fabrication of screen-printing pastes from TiO_2 powders for dye-sensitised solar cells. *Prog. Photovoltaics Res. Appl.* **2007**, *15*, 603−612.
(35) Lufaso, M. W.; Barnes, P. W.; Woodward, P. M. Structure prediction of ordered and disordered multiple octahedral cation perovskites using SPuDS. *Acta Crystallogr., Sect. B: Struct. Sci.* **2006**, *62*, 397−410.
(36) Woodward, P. M. Octahedral Tilting in Perovskites. I. Geometrical Considerations. *Acta Crystallogr., Sect. B: Struct. Crystallogr. Cryst. Chem.* **1997**, *53*, 32−43.
(37) Goldschmidt, V. M. Die gesetze der krystallochemie. *Naturwissenschaften* **1926**, *14*, 477−485.
(38) Kumar, A.; Verma, A. S.; Bhardwaj, S. R. Prediction of Formability in Perovskite-Type Oxides. *Open Appl. Phys. J.* **2008**, *1*, 11−19.
(39) Pilania, G.; Balachandran, P. V.; Gubernatis, J. E.; Lookman, T. Classification of ABO_3 perovskite solids: a machine learning study. *Acta Crystallogr., Sect. B: Struct. Sci., Cryst. Eng. Mater.* **2015**, *71*, 507−513.
(40) Pilania, G.; Balachandran, P. V.; Kim, C.; Lookman, T. Finding New Perovskite Halides via Machine Learning. *Front. Mater.* **2016**, *3*, 19.
(41) Slater, J. C. Atomic radii in crystals. *J. Chem. Phys.* **1964**, *41*, 3199−3204.
(42) Shannon, R. D.; Prewitt, C. T. Effective ionic radii in oxides and fluorides. *Acta Crystallogr., Sect. B: Struct. Crystallogr. Cryst. Chem.* **1969**, *25*, 925−946.
(43) King, G.; Woodward, P. M. Cation ordering in perovskites. *J. Mater. Chem.* **2010**, *20*, 5785.
(44) Saal, J. E.; Kirklin, S.; Aykol, M.; Meredig, B.; Wolverton, C. Materials Design and Discovery with High-Throughput Density Functional Theory: The Open Quantum Materials Database (OQMD). *JOM* **2013**, *65*, 1501−1509.
(45) Sun, W.; Dacek, S. T.; Ong, S. P.; Hautier, G.; Jain, A.; Richards, W. D.; Gamst, A. C.; Persson, K. A.; Ceder, G. The thermodynamic scale of inorganic crystalline metastability. *Sci. Adv.* **2016**, *2*, No. e1600225.
(46) Knapp, M. C.; Woodward, P. M. A-site cation ordering in $AA'BB'O_6$ perovskites. *J. Solid State Chem.* **2006**, *179*, 1076−1085.
(47) Howard, C. J.; Stokes, H. T. Structures and phase transitions in perovskites—a group-theoretical approach. *Acta Crystallogr., Sect. A: Found. Crystallogr.* **2005**, *61*, 93−111.
(48) Howard, C. J.; Kennedy, B. J.; Woodward, P. M. Ordered double perovskites - a group-theoretical analysis. *Acta Crystallogr., Sect. B: Struct. Sci., Cryst. Eng. Mater.* **2003**, *59*, 463−471.
(49) Heyd, J.; Scuseria, G. E.; Ernzerhof, M. Hybrid functionals based on a screened Coulomb potential. *J. Chem. Phys.* **2003**, *118*, 8207−8215.
(50) Heyd, J.; Scuseria, G. E.; Ernzerhof, M. "Hybrid functionals based on a screened Coulomb potential". *J. Chem. Phys.* **2003**, *118*, 8207.
(51) Morales-García, Á.; Valero, R.; Illas, F. An Empirical, yet Practical Way To Predict the Band Gap in Solids by Using Density Functional Band Structure Calculations. *J. Phys. Chem. C* **2017**, *121*, 18862−18866.
(52) Ha, V.-A.; Waroquiers, D.; Rignanese, G.-M.; Hautier, G. Influence of the "second gap" on the transparency of transparent conducting oxides: An ab initio study. *Appl. Phys. Lett.* **2016**, *108*, 201902.
(53) Pennycook, S. J.; Jesson, D. E. High-resolution Z-contrast imaging of crystals. *Ultramicroscopy* **1991**, *37*, 14−38.
(54) Wu, C.; Zhang, Q.; Liu, Y.; Luo, W.; Guo, X.; Huang, Z.; Ting, H.; Sun, W.; Zhong, X.; Wei, S.; Wang, S.; Chen, Z.; Xiao, L. The Dawn of Lead-Free Perovskite Solar Cell: Highly Stable Double Perovskite $Cs_2AgBiBr_6$ Film. *Adv. Sci.* **2018**, *5*, 1700759.
(55) Park, B.-W.; Philippe, B.; Zhang, X.; Rensmo, H.; Boschloo, G.; Johansson, E. M. J. Bismuth Based Hybrid Perovskites $A_3Bi_2I_9$ (A: Methylammonium or Cesium) for Solar Cell Application. *Adv. Mater.* **2015**, *27*, 6806−6813.

DOI: 10.1021/acs.chemmater.9b01025
Chem. Mater. 2019, 31, 4769−4778

(56) Yu, L.; Zunger, A. Identification of potential photovoltaic absorbers based on first-principles spectroscopic screening of materials. *Phys. Rev. Lett.* **2012**, *108*, 068701.
(57) Reference Air Mass 1.5 Spectra. https://www.nrel.gov/grid/solar-resource/spectra-am1.5.html (Accessed on March 12, 2019).
(58) Janotti, A.; Van de Walle, C. G. Native point defects in ZnO. *Phys. Rev. B: Condens. Matter Mater. Phys.* **2007**, *76*, 165202.
(59) Kavadiya, S.; Niedzwiedzki, D. M.; Huang, S.; Biswas, P. Electrospray-Assisted Fabrication of Moisture-Resistant and Highly Stable Perovskite Solar Cells at Ambient Conditions. *Adv. Energy Mater.* **2017**, *7*, 1700210.
(60) Yum, J.-H.; Chen, P.; Grätzel, M.; Nazeeruddin, M. K. Recent Developments in Solid-State Dye-Sensitized Solar Cells. *ChemSusChem* **2008**, *1*, 699−707.

DOI: 10.1021/acs.chemmater.9b01025
Chem. Mater. 2019, 31, 4769−4778